

# Metal–Semiconductor Phase-Transition in $WSe_{2(1-x)}Te_{2x}$ Monolayer

Peng Yu, Junhao Lin, Linfeng Sun, Quang Luan Le, Xuechao Yu, Guanhui Gao, Chuang-Han Hsu, Di Wu, Tay-Rong Chang, Qingsheng Zeng, Fucai Liu, Qi Jie Wang, Horng-Tay Jeng, Hsin Lin, Achim Trampert, Zexiang Shen, Kazu Suenaga, and Zheng Liu\*

In order to produce tunable high-performance electronic devices, band-gap engineering by alloying different semiconductors have been demonstrated in the bulk semiconductors,<sup>[1,2]</sup> such as  $Al_xGa_{1-x}As$  for quantum structures,  $CuIn_xGa_{1-x}Se_2$  for solar cells,  $In_xGa_{1-x}N$  for light emitting diodes, and  $Hg_xCd_{1-x}Te$  for infrared detectors, respectively. Recently, the band-gap engineering has been realized in monolayer ternary transitional metal dichalcogenides (TMDs) with 2H phase. For example, alloy  $MoS_{2x}Se_{2(1-x)}$  monolayer<sup>[3–6]</sup> with tunable chemical composition has been realized, as well as the  $W_xMo_{1-x}S_2$  and  $W_xMo_{1-x}Se_2$ .<sup>[6–9]</sup> However, only a few hundred milli-electron volts (meV) can be tuned for these ternary layers,  $\approx 300$  meV for  $W_xMo_{1-x}S_2$  and  $\approx 500$  meV for  $MoS_{2x}Se_{2(1-x)}$ ,<sup>[3–7]</sup> to be precise. Recently, the transition from semiconducting to metallic 2D  $MoTe_2$  has been reported by realizing a ultralow contact resistance at the heterostructured interface of 2H and

1Td  $MoTe_2$ .<sup>[10]</sup> These works inspire the synthesis of novel 2D materials with metal–semiconductor transition for applications in nanoelectronics and nanophotonics. Therefore, a unique ternary 2D material with tunable semiconductor–metal transition, preferably controlled by its chemical composition or ternary ratio, is urgently required to fill such gap. It is well known that  $WSe_2$  is a p-type 2D semiconductor with an indirect band gap (1.2 eV) for bulk and direct band gap (1.65 eV) for monolayer, respectively.<sup>[11–16]</sup> It generally shows 2H crystal structure. On the other hand,  $WTe_2$  is a semimetal with 1Td crystal structure, displaying an extremely large magnetoresistance effect in its diamagnetic single crystals.<sup>[17–21]</sup> The marriage of these two materials suggests a possible route for creating a ternary TMD layer to realize a semiconductor–metal phase transition.

In this work, ternary  $WSe_{2(1-x)}Te_{2x}$  ( $x = 0–1$ ) have been synthesized via chemical vapor transport (CVT) in a one-step synthesis, which exhibit two distinct structures (2H and 1Td, corresponding to semiconductor and metal, respectively). Three regions (2H phase, the coexistence of 2H and 1Td phase, and 1Td phase) have been identified in the complete composition of the alloy. Energy dispersive X-ray (EDX) and X-ray photoelectron spectroscopy (XPS) characterization confirm the existence of W, Se, and Te with a controlled ratio. Atomic resolution scanning transmission electron microscope (STEM) images further reveal the atomic structure of the alloyed monolayers with different Te alloying concentrations and how they evolve from 2H to the distorted 2H phase, and finally reshape into 1Td phase. Raman spectra identify different phases (2H and 1Td phases) and composition variations in the  $WSe_{2(1-x)}Te_{2x}$  alloy. The optical band gap of 2H  $WSe_{2(1-x)}Te_{2x}$  monolayer has been estimated by photoluminescence (PL) spectra. The electrical properties of atomic layered 2H  $WSe_2$ , 2H  $WSe_{1.4}Te_{0.6}$ , 1Td  $WSe_{0.6}Te_{1.4}$ , and 1Td  $WTe_2$  field-effect transistors (FETs) have been systematically studied, which indicates that 2H phase is p-type semiconductor and 1Td phase is a metal. Additionally, the p-type  $WSe_{2(1-x)}Te_{2x}$  FETs exhibit excellent electronic characteristic with effective hole carrier mobility up to  $46 \text{ cm}^2 \text{ V}^{-1} \text{ s}^{-1}$  and on/off ratios up to  $10^6$ .

The single crystals of  $WSe_{2(1-x)}Te_{2x}$  ( $x = 0–1.0$ ) alloys have been synthesized by the method of CVT with a small amount of iodine (I) as the transport agency, shown in Figure S1 (Supporting Information). It is noted that 2H and 1Td  $WSe_{2(1-x)}Te_{2x}$  single crystals form into platelets and strips, respectively, which are in agreement with their own crystalline space groups (hexagonal  $P6_3/mmc$  and orthorhombic  $Pmn2_1$ , respectively), as shown in Figure 1a.<sup>[11,17]</sup> The crystal structure of 2H  $WSe_{2(1-x)}Te_{2x}$  is similar to 2H  $MoS_2$ . It consists of the

Dr. P. Yu, Q. L. Le, Dr. Q. Zeng, Dr. F. Liu, Prof. Z. Liu  
School of Materials Science and Engineering  
Nanyang Technological University  
50 Nanyang Avenue, Singapore 639798, Singapore  
E-mail: Z.LIU@ntu.edu.sg

Dr. J. Lin, Prof. K. Suenaga  
National Institute of Advanced Industrial Science  
and Technology (AIST)  
Tsukuba 305-8565, Japan

Dr. L. Sun, Prof. Z. Shen  
School of Physical and Mathematical Sciences  
Nanyang Technological University  
50 Nanyang Avenue, Singapore 639798, Singapore

Dr. X. Yu, Prof. Q. J. Wang  
School of Electrical and Electronic Engineering  
Nanyang Technological University  
50 Nanyang Avenue, Singapore 639798, Singapore

Dr. G. Gao, Prof. A. Trampert  
Paul-Drude-Institut für Festkörperelektronik Leibniz-Institut im  
Forschungsverbund Berlin Hausvogteiplatz 5-7  
10117 Berlin, Germany

C.-H. Hsu, D. Wu, Prof. H. Lin  
Department of Physics  
National University of Singapore  
117542, Singapore

T.-R. Chang, H.-T. Jeng  
Department of Physics  
National Tsing Hua University  
Hsinchu 30013, Taiwan

H.-T. Jeng  
Institute of Physics  
Academia Sinica  
Taipei 11529, Taiwan



DOI: 10.1002/adma.201603991

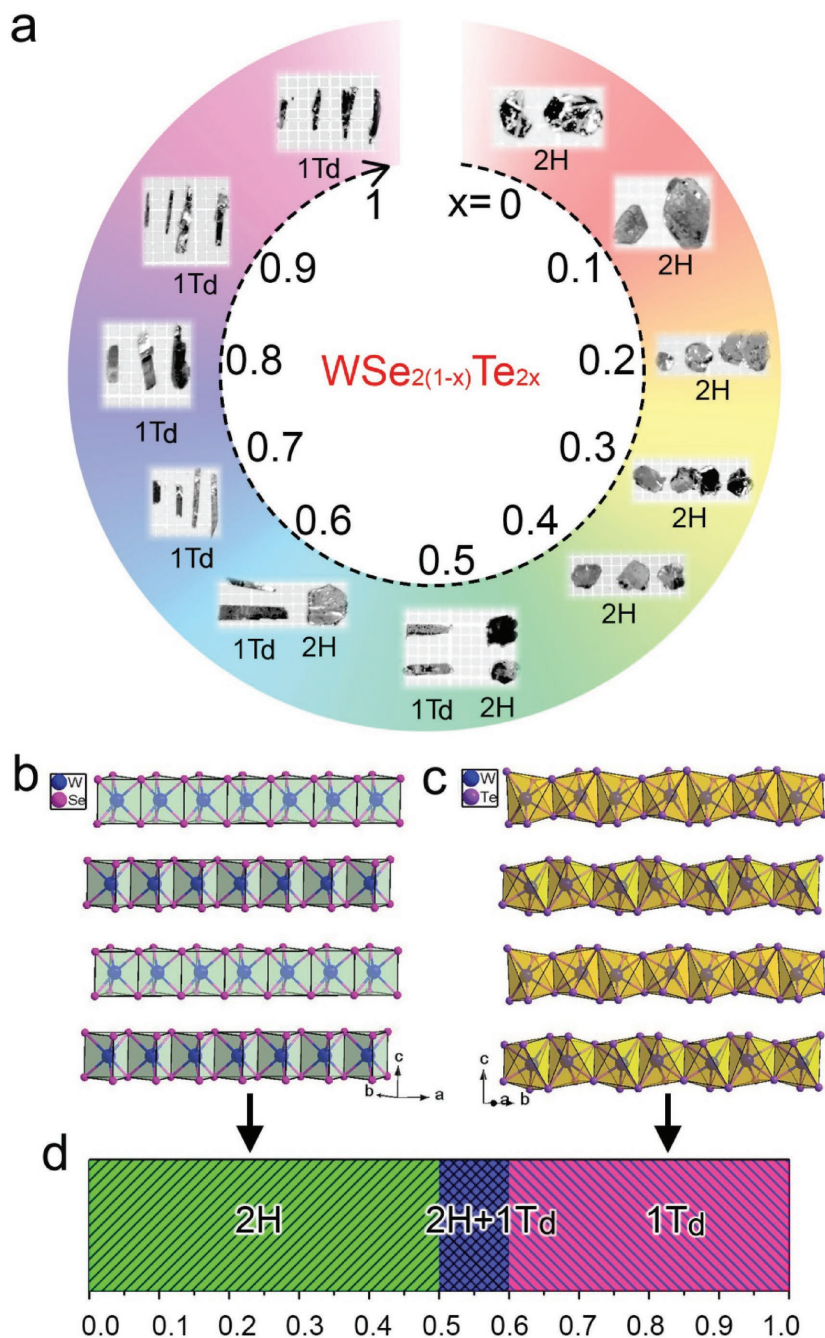


**Figure 1.** Morphologies of as-grown  $WSe_{2(1-x)}Te_{2x}$  ( $x = 0-1$ ) alloys. a) Photographs of as-grown  $WSe_{2(1-x)}Te_{2x}$  ( $x = 0-1$ ) single crystals on the millimeter-grid paper, and 2H and 1Td types TMD alloys show circularly platy and bar shapes, which are in agreement with hexagonal and orthorhombic crystal systems, respectively. b) The crystal structure of 2H  $WSe_2$ . c) The crystal structure of 1Td  $WTe_2$ . d) Different phases with dependence of concentration  $x$  in  $WSe_{2(1-x)}Te_{2x}$ .

$WSe_6$  or  $WSe/Te_6$  triangular prism layers bonded together by weak van der Waals forces, as shown in Figure 1b. While 1Td  $WSe_{2(1-x)}Te_{2x}$  is composed of the  $WTe_6$  or  $WSe/Te_6$  octahedra linked with each other by sharing the Te-Te edges. Its crystal structure shows a distorted variant of the 1T  $CdI_2$  type, regard as 1Td TMD structure shown in Figure 1c. As summarized in Figure 1d, the 2H and 1Td  $WSe_{2(1-x)}Te_{2x}$  can be produced

by tuning the concentration of Te from 0% to 100% where  $x = 0-0.4$  for 2H structure,  $x = 0.5$  and  $0.6$  for 2H and 1Td structures, and  $x = 0.7-1.0$  for 1Td structure, confirmed by EDX spectroscopy (EDXS) (Figure S2, Supporting Information), XPS (Figures S3-S6, Supporting Information), and the powder X-ray diffraction (Figure 1d and Figure S7, Supporting Information). It is worth noting that an intermediate state appears with two phases (1Td and 2H) when the concentration of Te increases.

The atomic structure of the layered  $WSe_{2(1-x)}Te_{2x}$  alloys has been further studied by Z-contrast STEM. Since the image intensity in Z-contrast STEM imaging is directly related to the atomic number of the imaged species in thin flakes, we only examine the alloyed monolayers exfoliated from the bulk. Figure 2 shows four typical monolayers with different Te concentration and phases, including 2H  $WSe_2$  ( $x = 0$ , Figure 2a), 2H  $WSe_{2(1-x)}Te_{2x}$  ( $x = 0.5$ , Figure 2b), 1Td  $WSe_{2(1-x)}Te_{2x}$  ( $x = 0.5$ , Figure 2c), and 1Td  $WTe_2$  ( $x = 1$ , Figure 2d). In pristine  $WSe_2$  shown in Figure 2a, the monolayer maintains a hexagonal lattice shape, with alternating bright and less bright spots as W and  $Se_2$  atomic columns, respectively, similar to the other reports.<sup>[22]</sup> The fast Fourier transform (FFT) pattern further confirms the hexagonal nature of the lattice. Figure 2b shows a monolayer region exfoliated from 2H  $WSe_{1.0}Te_{1.0}$  bulk crystal, which displays a hexagonal lattice shape (confirmed by FFT pattern) but exhibits distinguishable atomic column intensity from the pristine  $WSe_2$ .  $Te_2$  columns (the brightest spots in Figure 2b) maintain higher intensity than the W columns due to their heavier atomic weight, while Te+Se and  $Se_2$  columns have lower intensity than W, which confirms the successful in-lattice substitution of Te atoms in the Se sites. It is notable that such intensity distribution is similar to the ternary  $MoS_{2x}Se_{2(1-x)}$  alloys.<sup>[5]</sup>

Figure 2c shows a monolayer region exfoliated from the 1Td phase bulk crystal with similar chemical composition in Figure 2b. The atomic resolution image confirms the transition from the 2H phase to 1Td, as verified by the zigzag-like chains. FFT pattern further shows the periodicity of the lattice change from hexagonal to orthorhombic. Te atoms, which can be distinguished by its higher intensity than Se atoms, are found to be substituted into either two asymmetric sites in the orthorhombic unit cell of the 1Td phase, as indicated by the structural model. As shown in Figure 2d, further increasing the Te concentration to 100% results in  $WTe_2$  in a perfect 1Td phase where the zigzag

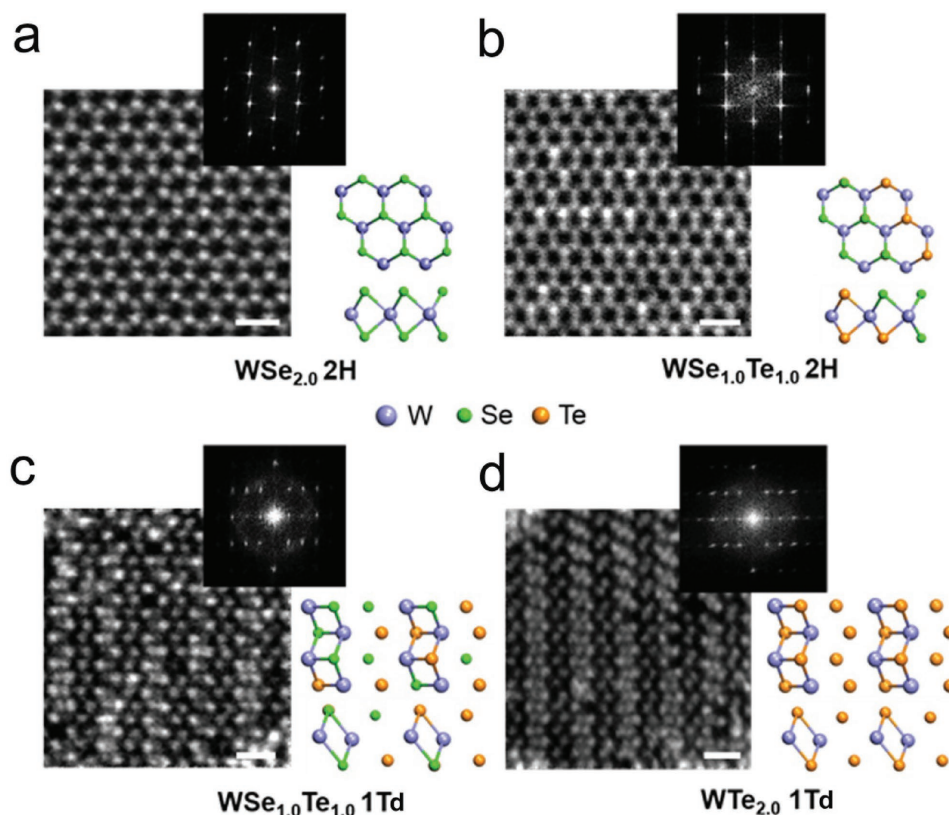


**Figure 2.** Atomic resolution STEM characterization of  $WSe_{2(1-x)}Te_{2x}$  ( $x = 0-1$ ) alloyed monolayers with different Te concentration. Z-contrast STEM images showing the atomic structure of a) pristine  $WSe_2$  monolayer in 2H phase, b) alloyed  $WSe_{1.0}Te_{1.0}$  monolayer in 2H phase, c) alloyed  $WSe_{1.0}Te_{1.0}$  monolayer in 1Td phase, and d) monolayer  $WTe_2$  in 1Td phase. Corresponding FFT patterns are shown in the inset.  $Te_2$ ,  $Te+Se$ , and  $Se_2$  atomic columns in the 2H phase, as well as the Te and Se atoms in the 1Td phase, can be distinguished by image intensity. The atomic models are just for schematic purpose. Scale bar: 0.5 nm.

W–Te and Te chains have uniform intensity distribution along the chain direction without much intensity variance, in sharp contrast to Figure 2c. Moreover, TEM characterizations of thick flakes of  $WSe_{2(1-x)}Te_{2x}$  with different Te concentrations are also provided in Figure S8 (Supporting Information). These results confirm the high quality of our as-synthesized bulk crystals. It is notable that although the high-resolution STEM results confirm the atomic structures of the coexisted 2H and 1Td phase in different  $WSe_{1.0}Te_{1.0}$  bulk crystal, we did not observe any intrinsic defect (such as dislocations or grain boundaries) except alloyed Te atoms and electron-induced vacancies in both the 2H and 1Td phases, neither phase segregation in the same flake. These results suggest that the phase transition may occur at the very beginning of the growth and continue to form perfect 2H or 1Td lattice structures depending on the initial nucleation. However, it is interesting that phase mixing (2H and 1Td) occurs at some critical range of Te alloy concentration, which requires more effort to investigate the phase transition mechanism inside these  $WSe_{2(1-x)}Te_{2x}$  alloys. This will be the topic of our future study of this material system.

Raman spectra of monolayer and bulk of  $WSe_{2(1-x)}Te_{2x}$  ( $x = 0\%-100\%$ ) single crystals have been collected to confirm the phase transformations in the sample with different Te compositions. The  $WSe_{2(1-x)}Te_{2x}$  monolayers are prepared by

micromechanical exfoliation of  $WSe_{2(1-x)}Te_{2x}$  single crystals and transfer their atomic layered samples on  $SiO_2/Si$  substrate (280 nm oxide layer) using the Scotch tape. The thicknesses of all the samples are identified by atomic force microscopy, as shown in Figure S10 (Supporting Information). Raman vibration modes dependent on the concentration of Te are mapped in Figure 3a,b, excited by 532 nm laser. For comparison, the typical Raman spectra of  $WSe_{2(1-x)}Te_{2x}$  for  $x = 0, 0.1, 0.2, 0.3, 0.4,$  and  $0.5$  are plotted in Figure 3c,d for monolayer and bulk samples, respectively. For  $WSe_2$ , the two characteristic peaks  $E^{1}_{2g}$  and  $A_{1g}$  for monolayer and bulk  $WSe_2$  are 248.6 and 260.9  $cm^{-1}$ , and 245.9 and 255.8  $cm^{-1}$ , respectively, in agreement with previous reports.<sup>[12,14,23–25]</sup> Increasing the concentration of Te softens these two peaks and make a redshift, as shown in Figure 3c, which can be contributed to the high-frequency vibration due to the heavy Te dopant. This phenomenon is also observed in other TMD alloy such as Se alloyed  $MoS_2$ . The intensity of the peaks becomes very weak. Meantime, for monolayer sample, the peak locates around 120  $cm^{-1}$  appears. It is also noticed that in both monolayer and bulk sample, after alloying Te,  $E^{1}_{2g}$  and  $A_{1g}$  vibration modes split into three modes as displayed in Figure 3c,d.

As we mentioned above (Figure 1), coexistence of 2H and 1Td phases occurs if the Te mole fraction in  $WSe_{2(1-x)}Te_{2x}$  alloy

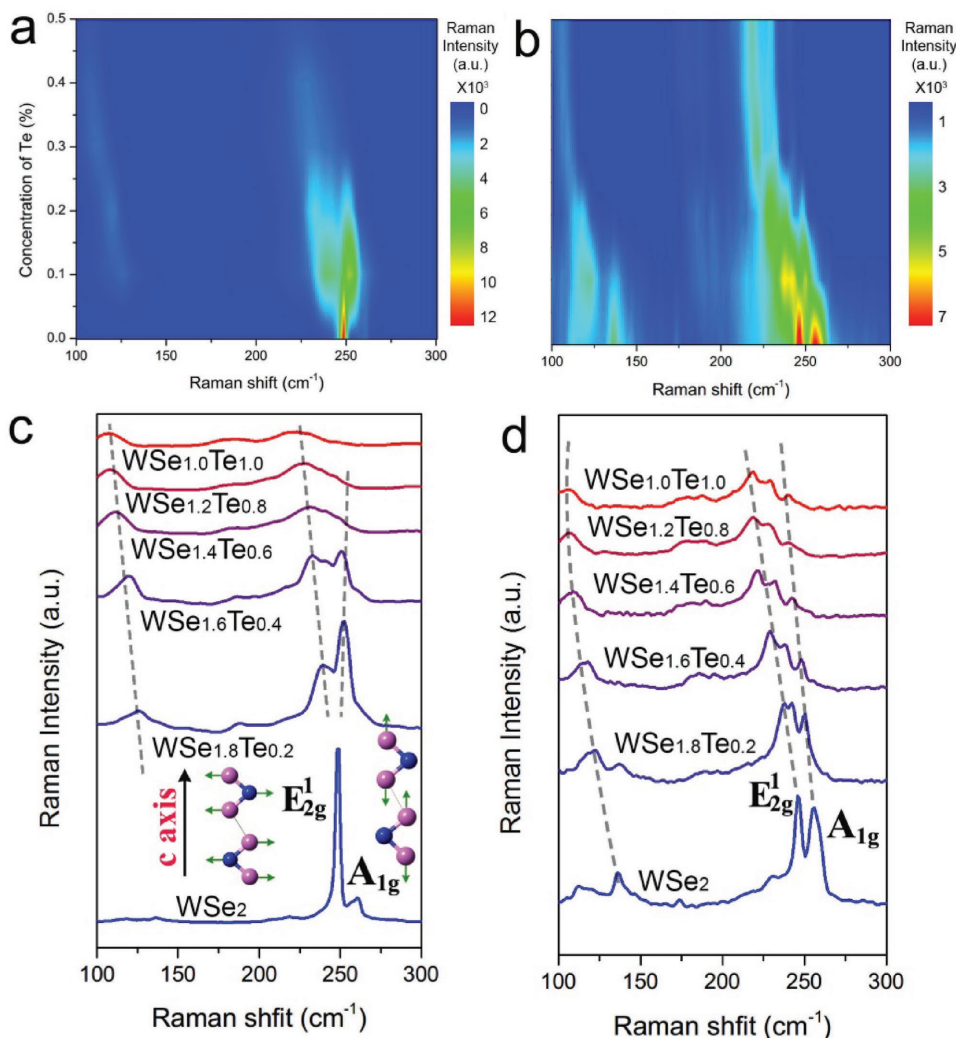


**Figure 3.** The Raman characterization of bulk and monolayer 2H  $WSe_{2(1-x)}Te_{2x}$  ( $x = 0-0.6$ ) alloys. Raman intensity of a) monolayer and b) bulk 2H  $WSe_{2(1-x)}Te_{2x}$  ( $x = 0-0.6$ ) alloys with the different Te compositions. Raman spectra of c) monolayer and d) bulk 2H  $WSe_{2(1-x)}Te_{2x}$  ( $x = 0-0.6$ ) alloys. The intensities of the W-Se related modes ( $E_{2g(W-Se)}^1$  and  $A_{1g(W-Se)}^1$ ) gradually decrease with Te mole fraction increases for monolayer and bulk samples, as shown in panels (a) and (b). Moreover, a redshift and splits of  $E_{2g(W-Se)}^1$  and  $A_{1g(W-Se)}^1$  vibration modes with Te mole fraction decreases happen.

is between 0.5 and 0.6, while only 1Td phase can be found in the samples when  $x > 0.6$ , a strong evidence that 2H phase is completely translated into 1Td phase in order to realize the transition from semiconductor to metal. In other words, the highest Se alloyed level in Te sites for 1Td  $WSe_{2(1-x)}Te_{2x}$  alloy is 0.4 in mole fraction. Such upper limit of Se dopant will be crucial for the studies of  $WTe_2$ -based Wyle semimetals via chalcogen alloying.<sup>[26-28]</sup> Also, it is interesting to examine the evolution of Raman signal of 1Td  $WSe_{2(1-x)}Te_{2x}$  ( $x \geq 0.5$ ). **Figure 4** shows the intensity of Raman vibration modes dependency on the mole fraction of Te and typical Raman spectra for monolayer and bulk 1Td  $WSe_{2(1-x)}Te_{2x}$  alloy, respectively. As shown in Figure 4a,b, two main vibration modes  $A_1^5$  and  $A_1^2$  (denoted as  $A_1^5$  and  $A_1^2$ , respectively) are found for monolayer and bulk  $WTe_2$  are 162.2 and 213.3  $cm^{-1}$ , and 161.17 and 208.60  $cm^{-1}$ , respectively, along with some weak peaks below 150  $cm^{-1}$ , which are in agreement with the reported values.<sup>[18,19]</sup> In

addition, in order to clearly show the signatures of the Raman signal, typical Raman spectra are plotted in Figure 4c,d ( $x = 0.5, 0.6, 0.7, 0.8, 0.9, \text{ and } 1.0$ ). Compared with the Raman peaks of bulk  $WTe_2$ , the peaks from monolayers show considerable blueshifts around 10  $cm^{-1}$ . More interestingly, Raman spectra of 1Td  $WSe_{2(1-x)}Te_{2x}$  alloys with  $x = 0.5$  and 0.6 display similar profiles. Such phenomenon is also observed in 2H  $WSe_{2(1-x)}Te_{2x}$  ( $x = 0.5$  and 0.6) alloys. Therefore, it is reasonable to speculate that  $WSe_{2(1-x)}Te_{2x}$  alloys with  $x = 0.5$  and 0.6 (mixture of 2H and 1Td) are intermediate states when the semiconducting 2H alloys transit to the metallic 1Td alloys. This is also supported by our STEM images in Figure 2b,c.

Engineering the band gap of 2D materials makes them the reality for the wide spectrum of applications. Recently, the carbon-doped boron nitride (BCN) films have been intensively studied so that ternary 2D materials become a promising way. However, the phase separation in BCN film at high temperature

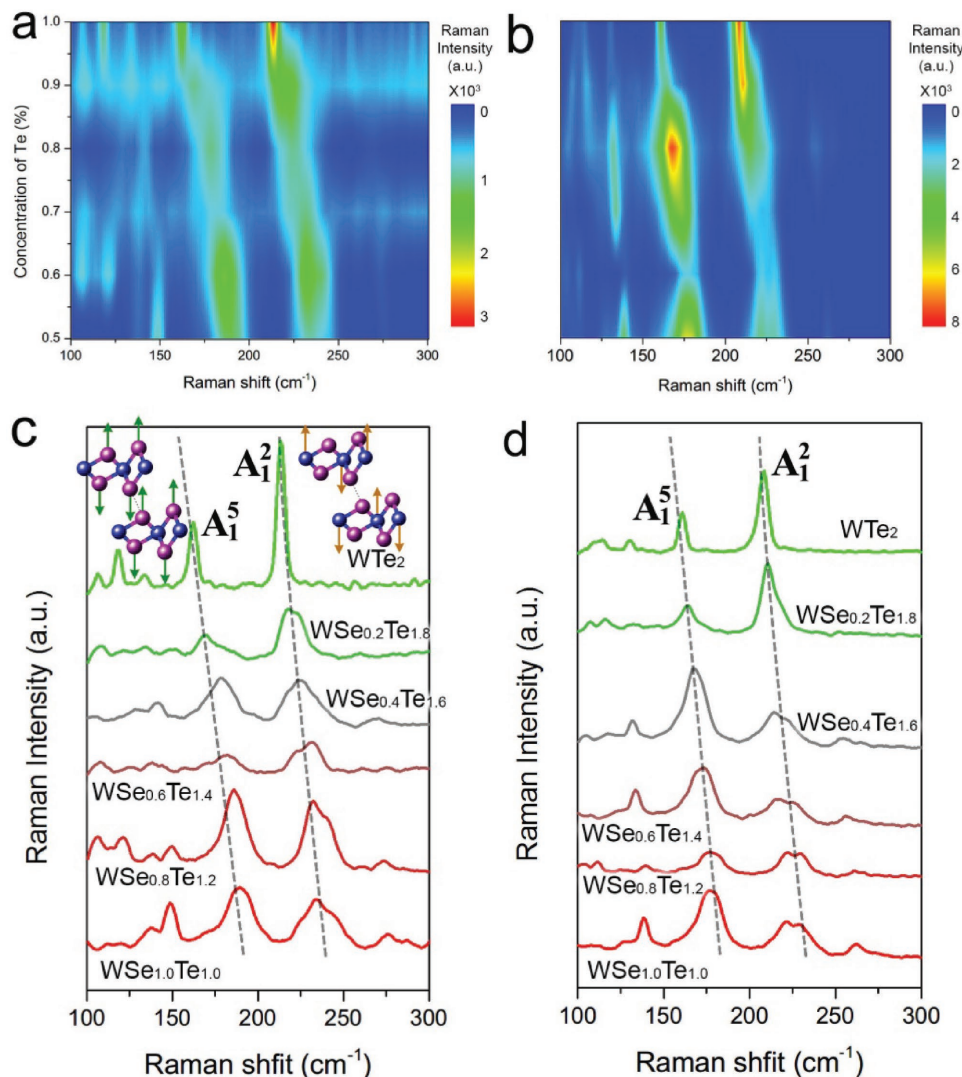


**Figure 4.** The Raman characterization of bulk and monolayer 1Td  $WSe_{2(1-x)}Te_{2x}$  ( $x = 0.6-1$ ) alloys with the different Te compositions. The intensities of the W–Te related vibration modes ( $A_{1(W-Te)}^5$  and  $A_{1(W-Te)}^2$ ) uniformly decrease with the concentration of Te increases from  $x = 0.6$  to 1 for monolayer and bulk. Raman spectra of c) monolayer and d) bulk 1Td  $WSe_{2(1-x)}Te_{2x}$  ( $x = 0.6-1$ ) alloys are shown, which show that the  $A_{1(W-Te)}^5$  and  $A_{1(W-Te)}^2$  vibration modes make a redshift and become sharp with the concentration of Te increases from  $x = 0.6$  to 1.

makes it a challenge to produce homogeneous BCN atomic layers with precious control in the composition, mainly due to the lattice mismatch of h-BN and graphene which is not low enough ( $\approx 2.7\%$ ). TMDs, consisting of a few families with similar crystal structure, make it possible to produce the homogeneous 2D ternary monolayers. TMD alloys, such as Se alloyed  $MoS_2$ , W alloyed  $MoS_2$ , etc., have been reported in the past few years.<sup>[3–9,29]</sup> But no TMD ternary can provide a transition from semiconductor to metal like what have been reported in BCN films and bulk materials. The  $WSe_{2(1-x)}Te_{2x}$ , consisting of semiconducting  $WSe_2$  ( $x = 0$ ) and metallic  $WTe_2$  ( $x = 1$ ), makes it possible to achieve a much large tunable range of band gap. PL is a good tool to evaluate the optical gap of semiconducting materials, especially band gaps evolution in 2H  $WSe_{2(1-x)}Te_{2x}$  ( $x = 0-0.6$ ). The PL spectra of monolayer samples excited with

a 532 nm laser are collected and shown in **Figure 5a**. All monolayer 2H  $WSe_{2(1-x)}Te_{2x}$  show the emission bands, and the spectral peak continuously shifts from 744 nm (pure  $WSe_2$ ) to 857 nm (near infrared). For 1Td sample, as expected, no PL signal is detected when  $x \geq 0.6$ . **Figure 5b** plots the optical gap versus mole fraction of Te for monolayer  $WSe_{2(1-x)}Te_{2x}$ . The band gaps are continuously shifted from 1.67 eV (pure  $WSe_2$ ) to 1.44 eV. Interestingly, it can be found that the optical gaps are similar when  $x = 0.5$  and 0.6, indicating that the highest concentration of Te dopant in 2H  $WSe_{2(1-x)}Te_{2x}$  alloy is 0.6, which is in well agreement with the Raman data. At the same time, the optical gap directly changes from 1.44 (2H semiconductor) to 0 eV (1Td metal) in this regime. The optical gaps are 0 eV when  $x > 0.6$ , confirming that the  $WSe_{2(1-x)}Te_{2x}$  alloys undergo a phase transition from semiconductor (2H phase) to metal

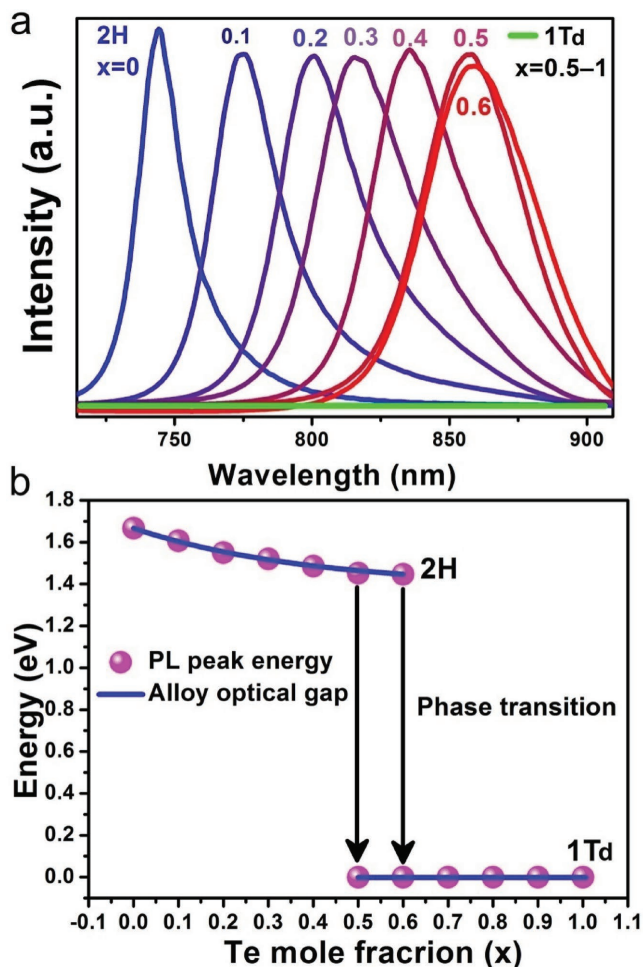


**Figure 5.** The photoluminescence (PL) spectra of monolayer  $\text{WSe}_{2(1-x)}\text{Te}_{2x}$  ( $x = 0-1.0$ ) alloys. a) The PL spectrum of the composition monolayer 2H  $\text{WSe}_{2(1-x)}\text{Te}_{2x}$  ( $x = 0-0.6$ ) alloys. b) The PL measurements of the composition monolayer 1Td  $\text{WSe}_{2(1-x)}\text{Te}_{2x}$  ( $x = 0.5-1.0$ ) alloys. c) Composition-dependent ( $x$ ) band gaps of the monolayer  $\text{WSe}_{2(1-x)}\text{Te}_{2x}$  ( $x = 0-0.6$ ) alloys.

(1Td phase). The band gaps of 2H  $\text{WSe}_{2(1-x)}\text{Te}_{2x}$  ( $x = 0-0.6$ ) monolayers, bilayers, and bulk are calculated in Figure S11 (Supporting Information), basically consistent with our experimental result. In addition, the calculated results also show that 2H Te alloyed  $\text{WSe}_2$  monolayer is a direct-gap semiconductor and 1Td  $\text{WTe}_2$  monolayer is metallic (Figures S12 and S13, Supporting Information). Interestingly, the strong optical second harmonic generation (SHG) is found in 2H  $\text{WSe}_2$ , 2H  $\text{WSe}_{1.8}\text{Te}_{0.2}$ , 2H  $\text{WSe}_{1.4}\text{Te}_{0.6}$ , and 2H  $\text{WSe}_{1.2}\text{Te}_{0.8}$  monolayers (Figure S14, Supporting Information), which shows that the break of inversion symmetry happens in monolayer. With the increase of the mole fraction of Te, the intensities of SHG become weaker, which may be ascribed to the differences of the polarization or the absorbency of the samples with the different concentration of Te. The SHG polarization dependence of 2H  $\text{WSe}_2$  and 2H  $\text{WSe}_{1.4}\text{Te}_{0.6}$  monolayers (Figures S15 and S16, Supporting Information) is also investigated, which shows that the samples display three-fold rotational symmetry, in accordance with the  $D_{3h}$  symmetry.<sup>[30-32]</sup>

The FET devices based bilayer 2H  $\text{WSe}_{2(1-x)}\text{Te}_{2x}$  ( $x = 0$  and 0.3) and 1Td  $\text{WSe}_{2(1-x)}\text{Te}_{2x}$  ( $x = 0.7$  and 1) have been fabricated on  $\text{SiO}_2/\text{Si}$  (280 nm oxide layer) substrate in order to further confirm the semiconducting 2H phases and metallic 1Td phases. The Ti/Au electrodes are deposited by e-beam evaporation after photolithography (Figure S17, Supporting Information). The optical images of devices are shown in the center of Figure 6. The current-voltage ( $I_{\text{ds}}-V_{\text{ds}}$ ) curve and the transfer characteristics ( $I_{\text{ds}}-V_{\text{bg}}$ ) of the  $\text{WSe}_{2(1-x)}\text{Te}_{2x}$  transistors are displayed in Figure 6a-g. By increasing the alloyed level of Te from 0 to 0.3, the drain current increases from around 1.7 to 15 nA at a drain voltage of 2V and no gating voltage. The transfer characteristics clearly show a p-type semiconducting behavior for both samples, consistent with the theoretical results and previous literatures.<sup>[12,13,33]</sup> The mobility of the carriers can be calculated by

$$\mu = \frac{L}{W \times (\epsilon_0 \epsilon_r / d)} \times \frac{dI_{\text{ds}}}{dV_{\text{g}}} \times \frac{1}{V_{\text{ds}}}$$

where  $L$ ,  $W$ , and  $d$  denote the channel length, width, and the thickness of  $\text{SiO}_2$  layer (285 nm in our devices), respectively.<sup>[34]</sup>  $V_{\text{ds}}$ ,  $I_{\text{ds}}$ , and  $V_{\text{b}}$  denote the source-drain bias, current, and bottom gate voltage in the linear region in the  $I_{\text{ds}}-V_{\text{g}}$  curve.  $\epsilon_0$  and  $\epsilon_r$  are the vacuum dielectric constant and the dielectric constant of  $\text{SiO}_2$  ( $\epsilon_r = 3.9$ ), respectively. The calculated mobility and on/off ratio of bilayer 2H  $\text{WSe}_{2(1-x)}\text{Te}_{2x}$  for  $x = 0$  and 0.3 are  $10 \text{ cm}^2\text{V}^{-1}\text{s}^{-1}$  and  $10^6$ , and  $46 \text{ cm}^2\text{V}^{-1}\text{s}^{-1}$  and  $10^6$ , respectively. For  $x = 0.7$  and 1.0, as expected, no drain current dependency is found on the gating voltage, suggesting that 1Td  $\text{WTe}_2$  and  $\text{WSe}_{0.6}\text{Te}_{1.4}$  are metallic. It is also noticed that, for  $x = 0.7$ , the drain current is around 20 nA at a drain voltage of 2V. For  $x = 1.0$ , that is pure  $\text{WTe}_2$ , the drain current increases more than 3 orders of magnitude, reach to around 40  $\mu\text{A}$ . It indicates that the metallic behavior of  $\text{WTe}_2$  could be considerably impacted by alloying Se. In addition, the plots of the resistance with the dependence of temperature (Figure S18, Supporting Information) also confirm that 2H  $\text{WSe}_{2(1-x)}\text{Te}_{2x}$  ( $x = 0$  and 0.3) are semiconductors and 1Td  $\text{WSe}_{2(1-x)}\text{Te}_{2x}$  ( $x = 0.7$  and 1) are metals because the resistances decrease with increasing temperature for the former, but increase with increasing temperature for the latter.

In conclusion, the phase transition of TMD monolayer from semiconductor to metal has been demonstrated by alloying Te into tungsten diselenide. Using one-step CVT, the complete composition of  $\text{WSe}_{2(1-x)}\text{Te}_{2x}$  ( $x = 0-1$ ) alloys is obtained, which exhibit distinguishable semiconducting 2H and metallic 1Td phase. Three regions (2H phase, the coexistence of 2H and 1Td phase, and 1Td phase) are identified in the complete composition of  $\text{WSe}_{2(1-x)}\text{Te}_{2x}$  ( $x = 0-1$ ) alloy using EDXS and Raman spectroscopy. STEM images clearly confirm the semiconducting and metallic  $\text{WSe}_{2(1-x)}\text{Te}_{2x}$  alloys showing the hexagonal and orthorhombic lattices, respectively, and the random distribution nature of the Se and Te atoms arrangements in these alloys is also found. The PL spectra show that the optical band gaps of the  $\text{WSe}_{2(1-x)}\text{Te}_{2x}$  monolayer can be tuned from 1.67 to 1.44 eV (2H semiconductor) and drop to 0 eV (1Td metal). Additionally,  $\text{WSe}_{2(1-x)}\text{Te}_{2x}$  atomic layer based FET devices confirm that 2H phase is p-type semiconductor but 1Td phase is metal. It is noted that the p-type bilayer 2H  $\text{WSe}_2$  and 2H  $\text{WSe}_{1.4}\text{Te}_{0.6}$  FETs exhibit excellent electronic characteristic with effective hole carrier mobility up to 10 and  $46 \text{ cm}^2\text{V}^{-1}\text{s}^{-1}$  and on/off ratios up to  $10^6$ , respectively. These band-gap engineering 2D structures

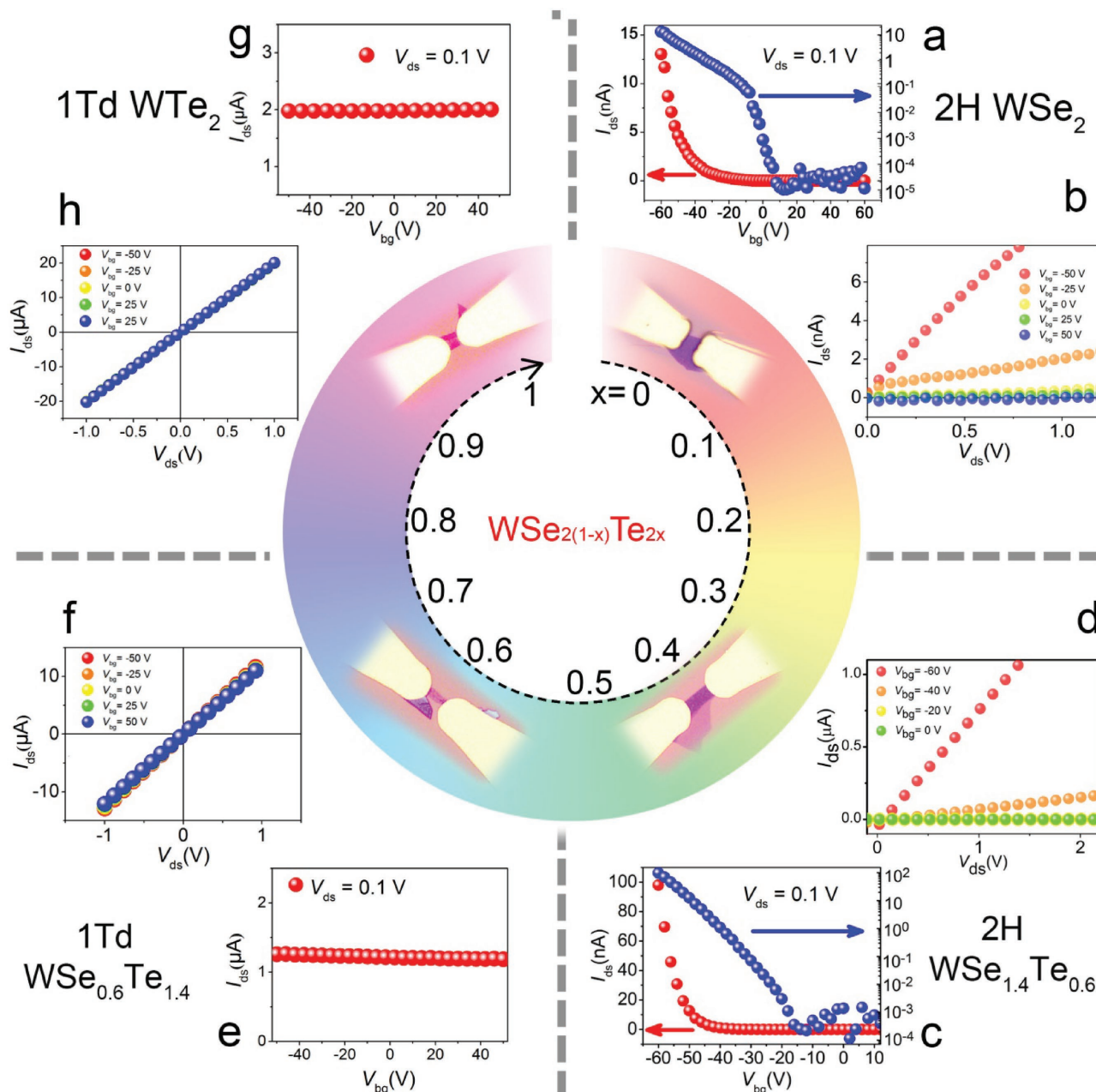


**Figure 6.** The electrical property of the fabricated 2H  $WSe_{2(1-x)}Te_{2x}$  ( $x = 0, 0.3$ ) and 1Td  $WSe_{2(1-x)}Te_{2x}$  ( $x = 0.7, 1$ ) bilayer FET. Gating response ( $I_{ds}-V_{bg}$ ) with a source-drain voltage ( $V_{ds}$ ) of 0.1 V and the current-voltage ( $I_{ds}-V_{ds}$ ) curves with different bottom gate voltage of a,b) 2H  $WSe_2$ , c,d) 2H  $WSe_{1.4}Te_{0.6}$ , e,f) 1Td  $WSe_{0.6}Te_{1.4}$ , and g,h) 1Td  $WTe_2$  bilayer FETs, whose optical images of the fabricated device are shown in the circular ring, respectively.

could open up an exciting opportunity not only for probing their fundamental physical properties in 2D such as new type of Wyle semimetals and spin Hall effect but also for diverse applications in functional electronic/optoelectronic devices.

### Experimental Section

**Synthesis and Mechanical Exfoliation of  $WSe_{2(1-x)}Te_{2x}$  ( $x = 0-1$ ) Single Crystals:** Single crystals of  $WSe_{2(1-x)}Te_{2x}$  ( $x = 0-1$ ) were prepared by the method of CVT with iodine as the transporting agency. The stoichiometric

amounts of high purity W, Te, and Se with the weight of 0.3 g and 40 mg iodide were sealed in an evacuated 20 cm long quartz tube under vacuum at  $10^{-6}$  Torr, which was placed in a three-zone furnace. The reaction zone was pretreated at  $850^\circ\text{C}$  for 30 h with the grown zone at  $900^\circ\text{C}$ , preventing the transport of the samples. The reaction zone was then programmed at a higher temperature of  $1010^\circ\text{C}$  with the growth zone at a lower temperature of  $900^\circ\text{C}$  for 3 d to provide a temperature gradient for the growth of single crystal. Finally, the furnace was naturally cooled down to room temperature and the single crystal of  $WSe_{2(1-x)}Te_{2x}$  ( $x = 0-1$ ) can be collected in the growth zone. 2H and 1Td  $WSe_{2(1-x)}Te_{2x}$  single crystals show different shapes with the platelet and ribbon, respectively, shown in Figure 1a. Monolayer  $WSe_{2(1-x)}Te_{2x}$  ( $x = 0-1$ )

was mechanically exfoliated from bulk  $\text{WSe}_{2(1-x)}\text{Te}_{2x}$  single crystals and transferred to a silicon substrate with a 280 nm thick silica layer using the scotch tape based mechanical exfoliation method, which was widely employed for the preparation of monolayer graphene and transitional metal dichalcogenides (TMDs).

**TEM Sample Preparations and Image Simulations:** The synthesis of  $\text{WSe}_{2(1-x)}\text{Te}_{2x}$  ( $x = 0.5-0.6$ ) yielded out samples with two distinct morphologies (2H and 1Td phase). The TEM samples of 2H and 1Td phases were fabricated by exfoliating the corresponding bulk crystals (different shape) separately, and then the exfoliated flakes were transferred onto Au grid with carbon film via a conventional wet-transfer method with the assistance of PMMA. The Z-contrast STEM imaging was done with a modified JEOL 2100F with delta probe corrector, which corrects the aberration up to fifth order, resulting in a probe size of 1.4 Å. The imaging was conducted at an acceleration voltage of 60 kV. The convergent angle for illumination was about 35 mrad, with a collection detector angle ranging from 62 to 200 mrad.

**The Fabrication and Measurements of the Devices:** The devices were fabricated by photolithography and Ti/Au or Ti/Cr (20 nm/80 nm) as contact electrodes were deposited using electron-beam evaporation. The channel lengths and widths of the fabricated devices were 6 and 7  $\mu\text{m}$  for 2H  $\text{WSe}_2$ , 8 and 5  $\mu\text{m}$  for 2H  $\text{WSe}_{1.4}\text{Te}_{0.6}$ , 6 and 4  $\mu\text{m}$  for 1Td  $\text{WSe}_{0.6}\text{Te}_{1.4}$ , and 6 and 5  $\mu\text{m}$  for 1Td  $\text{WTe}_2$ . The final devices were annealed at 400 °C for 2 h with the protection of nitrogen in order to remove resist residues and enhance the metallic contacts. Electrical characterization was performed by current–voltage measurements on a probe station equipped with a semiconductor characterization system AgilentB1500A.

## Supporting Information

Supporting Information is available from the Wiley Online Library or from the author.

## Acknowledgements

P.Y. and J.L. contributed equally to this work. This work was supported by the National Research Foundation Singapore under NRF RF Award No. NRF-RF2013-08. This work was also supported by MOE2011-T2-2-147, MOE2011-T3-1-005 and MOE2015-T2-2-007 from Ministry of Education, Singapore, and CoE Industry Collaboration Grant (WINTeCH-NTU-LIU). J.L. and K.S. acknowledge support from the JST Research Acceleration Program. H.L. acknowledges the Singapore National Research Foundation for the support under NRF Award No. NRF-NRFF2013-03.

Received: July 27, 2016

Revised: September 12, 2016

Published online: November 22, 2016

- [1] S. H. Wei, A. Zunger, *J. Appl. Phys.* **1995**, *78*, 3846.
- [2] S.-H. Wei, S. B. Zhang, A. Zunger, *J. Appl. Phys.* **2000**, *87*, 1304.
- [3] Q. Feng, Y. Zhu, J. Hong, M. Zhang, W. Duan, N. Mao, J. Wu, H. Xu, F. Dong, F. Lin, C. Jin, C. Wang, J. Zhang, L. Xie, *Adv. Mater.* **2014**, *26*, 2648.
- [4] H. Li, X. Duan, X. Wu, X. Zhuang, H. Zhou, Q. Zhang, X. Zhu, W. Hu, P. Ren, P. Guo, L. Ma, X. Fan, X. Wang, J. Xu, A. Pan, X. Duan, *J. Am. Chem. Soc.* **2014**, *136*, 3756.
- [5] Y. Gong, Z. Liu, A. R. Lupini, G. Shi, J. Lin, S. Najmaei, Z. Lin, A. L. Elías, A. Berkdemir, G. You, H. Terrones, M. Terrones, R. Vajtai, S. T. Pantelides, S. J. Pennycook, J. Lou, W. Zhou, P. M. Ajayan, *Nano Lett.* **2014**, *14*, 442.
- [6] Y. Chen, J. Xi, D. O. Dumcenco, Z. Liu, K. Suenaga, D. Wang, Z. Shuai, Y.-S. Huang, L. Xie, *ACS Nano* **2013**, *7*, 4610.
- [7] Y. Chen, D. O. Dumcenco, Y. Zhu, X. Zhang, N. Mao, Q. Feng, M. Zhang, J. Zhang, P.-H. Tan, Y.-S. Huang, L. Xie, *Nanoscale* **2014**, *6*, 2833.
- [8] D. O. Dumcenco, H. Kobayashi, Z. Liu, Y.-S. Huang, K. Suenaga, *Nat. Commun.* **2013**, *4*, 1351.
- [9] M. Zhang, J. Wu, Y. Zhu, D. O. Dumcenco, J. Hong, N. Mao, S. Deng, Y. Chen, Y. Yang, C. Jin, S. H. Chaki, Y.-S. Huang, J. Zhang, L. Xie, *ACS Nano* **2014**, *8*, 7130.
- [10] S. Cho, S. Kim, J. H. Kim, J. Zhao, J. Seok, D. H. Keum, J. Baik, D.-H. Choe, K. J. Chang, K. Suenaga, S. W. Kim, Y. H. Lee, H. Yang, *Science* **2015**, *349*, 625.
- [11] M. Xu, T. Liang, M. Shi, H. Chen, *Chem. Rev.* **2013**, *113*, 3766.
- [12] J.-K. Huang, J. Pu, C.-L. Hsu, M.-H. Chiu, Z.-Y. Juang, Y.-H. Chang, W.-H. Chang, Y. Iwasa, T. Takenobu, L.-J. Li, *ACS Nano* **2014**, *8*, 923.
- [13] H. Fang, S. Chuang, T. C. Chang, K. Takei, T. Takahashi, A. Javey, *Nano Lett.* **2012**, *12*, 3788.
- [14] W. Liu, J. Kang, D. Sarkar, Y. Khatami, D. Jena, K. Banerjee, *Nano Lett.* **2013**, *13*, 1983.
- [15] V. Podzorov, M. E. Gershenson, C. Kloc, R. Zeis, E. Bucher, *Appl. Phys. Lett.* **2004**, *84*, 3301.
- [16] C. Chiritescu, D. G. Cahill, N. Nguyen, D. Johnson, A. Bodapati, P. Keblinski, P. Zschack, *Science* **2007**, *315*, 351.
- [17] M. N. Ali, J. Xiong, S. Flynn, J. Tao, Q. D. Gibson, L. M. Schoop, T. Liang, N. Haldolaarachchige, M. Hirschberger, N. P. Ong, R. J. Cava, *Nature* **2014**, *514*, 205.
- [18] W.-D. Kong, S.-F. Wu, P. Richard, C.-S. Lian, J.-T. Wang, C.-L. Yang, Y.-G. Shi, H. Ding, *Appl. Phys. Lett.* **2015**, *106*, 081906.
- [19] Y. M. Jhon, Y. Kim, Y. I. Jhon, J. Park, J. H. Kim, S. Lee, *Nanoscale* **2016**, *8*, 2309.
- [20] I. Pletikosić, M. N. Ali, A. V. Fedorov, R. J. Cava, T. Valla, *Phys. Rev. Lett.* **2014**, *113*, 216601.
- [21] C.-H. Lee, E. C. Silva, L. Calderin, M. A. T. Nguyen, M. J. Hollander, B. Bersch, T. E. Mallouk, J. A. Robinson, *Sci. Rep.* **2015**, *5*, 10013.
- [22] Y. Gong, G. Ye, S. Lei, G. Shi, Y. He, J. Lin, X. Zhang, R. Vajtai, S. T. Pantelides, W. Zhou, B. Li, P. M. Ajayan, *Adv. Funct. Mater.* **2016**, *26*, 2009.
- [23] J. S. Ross, P. Klement, A. M. Jones, N. J. Ghimire, J. Yan, D. G. Mandrus, T. Taniguchi, K. Watanabe, K. Kitamura, W. Yao, D. H. Cobden, X. Xu, *Nat. Nanotechnol.* **2014**, *9*, 268.
- [24] W. Zhao, Z. Ghorannevis, K. K. Amara, J. R. Pang, M. Toh, X. Zhang, C. Kloc, P. H. Tan, G. Eda, *Nanoscale* **2013**, *5*, 9677.
- [25] S. B. Desai, G. Seol, J. S. Kang, H. Fang, C. Battaglia, R. Kapadia, J. W. Ager, J. Guo, A. Javey, *Nano Lett.* **2014**, *14*, 4592.
- [26] A. A. Soluyanov, D. Gresch, Z. Wang, Q. Wu, M. Troyer, X. Dai, B. A. Bernevig, *Nature* **2015**, *527*, 495.
- [27] Y. Wu, N. H. Jo, D. Mou, L. Huang, S. L. Bud'ko, P. C. Canfield, A. Kaminski, *Phys. Rev. B* **2016**, *94*, 12113.
- [28] C. Wang, Y. Zhang, J. Huang, S. Nie, G. Liu, A. Liang, Y. Zhang, B. Shen, J. Liu, C. Hu, Y. Ding, D. Liu, Y. Hu, S. He, L. Zhao, L. Yu, J. Hu, **2016**, arXiv:1604.04218.
- [29] J. Mann, Q. Ma, P. M. Odenthal, M. Isarraraz, D. Le, E. Preciado, D. Barroso, K. Yamaguchi, G. von Son Palacio, A. Nguyen, T. Tran, M. Wurch, A. Nguyen, Y. Klee, S. Bobek, D. Sun, T. F. Heinz, T. S. Rahman, R. Kawakami, L. Bartels, *Adv. Mater.* **2014**, *26*, 1399.
- [30] Y. Li, Y. Rao, K. F. Mak, Y. You, S. Wang, C. R. Dean, T. F. Heinz, *Nano Lett.* **2013**, *13*, 3329.
- [31] N. Kumar, S. Najmaei, Q. Cui, F. Ceballos, P. M. Ajayan, J. Lou, H. Zhao, *Phys. Rev. B* **2013**, *87*, 161403.
- [32] K. L. Seyler, J. R. Schaibley, P. Gong, P. Rivera, A. M. Jones, S. Wu, J. Yan, D. G. Mandrus, W. Yao, X. Xu, *Nat. Nanotechnol.* **2015**, *10*, 407.
- [33] H. Zhou, C. Wang, J. C. Shaw, R. Cheng, Y. Chen, X. Huang, Y. Liu, N. O. Weiss, Z. Lin, Y. Huang, X. Duan, *Nano Lett.* **2015**, *15*, 709.
- [34] X. Liu, J. Hu, C. Yue, N. Della Fera, Y. Ling, Z. Mao, J. Wei, *ACS Nano* **2014**, *8*, 10396.